2024 IEEE International Conference on Robotics and Automation (ICRA 2024)
May 13-17, 2024. Yokohama, Japan

Lissajous Curve-Based Vibrational Orbit Control of a Flexible Vibrational Actuator with a Structural Anisotropy

Yuto Miyazaki and Mitsuru Higashimori

***Abstract*— This paper proposes a novel flexible vibrational actuator with a structural anisotropy and its control method to diversify the vibrational behavior. First, the analytical model of the proposed actuator, which comprises a rectangular cross-sectional flexible beam and a rotational-type motor, is introduced. Regarding the structural anisotropy, the rotational axis of the motor is nonparallel to both principal axes of bending stiffness of the beam. Then, the vibrational phenomenon of the actuator is theoretically revealed. It is shown that using the synthetic wave input constituting two sine waves based on the resonance frequencies for the principal axes of the beam, the vibrational orbit of the tip of the beam can be controlled in the same manner as the Lissajous curve. Finally, the proposed method is experimentally validated. The Lissajous curve-based vibrational orbit control is performed using a prototype actuator. Furthermore, an application to underactuated-type locomotor is demonstrated.**

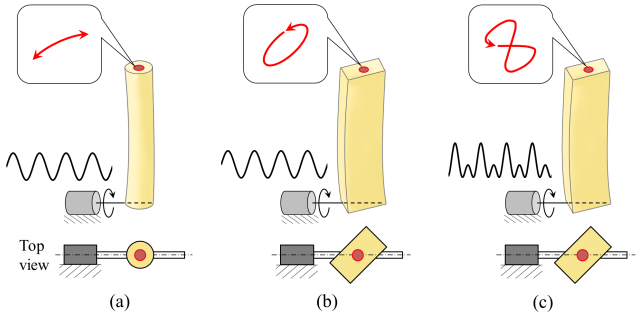

Fig. 1. Flexible vibrational actuator. (a) An isotropic type with a sine wave input. (b) An anisotropic type with a sine wave input. (c) An anisotropic type with a synthetic waveform input. The shape of vibrational orbit can be diversified drastically based on the principle of Lissajous curve.

I. Introduction

Soft and flexible robotics utilizing mechanical characteristics of soft or flexible materials have been actively studied [1]–[4]. Robots using dynamic shape change of soft or flexible body have been discussed. For example, the compliant humanoid robot (COMAN robot) [5] and the underwater locomotor using pulstile pump [6] have been designed and developed. However, these works focused on complicated control input. By actively utilizing mechanical characteristics of soft or flexible matters, simple sine wave input can cause various motions. For example, the locomotor using vibration of the twisted beam [8], the walking robot using vibration of soft 2D repetitive slit patterns [7], the underwater swimming robot using an anisotropy of buckling load of the curve-based beam [9], and the microrobot that moves using sound waves by placing its legs in a non-vertical direction [10] have been designed and developed. Regarding the above mentioned robots, it is important to note that the flexible body has structural asymmetry or anisotropy. When sine wave displacement or force input occures on the one tip of such a flexible body, the vibrational behavior varies according to the input frequency. With this behavior, the robot can perform locomotion or manipulation. The robot motion in a particular direction means that it breaks a spatial symmetry, caused by the structural asymmetry or anisotropy of the robot.

The authors' group has discussed the vibrational behavior of a flexible body with a structural anisotropy for the sine wave displacement input [11], and revealed the vibrational orbit varies with respect to the input frequency. For a cylindrical beam with a structural isotropy as shown in Fig. 1(a), the vibrational orbit of the tip is limited to arc-shaped orbits. In contrast, for a rectangular beam with a structural anisotropy as shown in Fig. 1(b), the shape of the vibrational orbit of the tip becomes elliptical due to a particular input frequency. Considering such a principle of vibrational orbit change, the authors have proposed the underactuated system in which the number of degrees of freedom of the tip motion is larger than the number of motors. Now, we consider employing synthetic wave input, as depicted in Fig. 1(c). In this case, the vibrational orbit, which is integrated in the vibrational component by the first sine wave and that by the second sine wave, is generated. It is expected that, with appropriate parameters of two sine waves based on the beam structure, the vibrational orbit can be drastically diversified.

Based on the above background, this paper presents a novel flexible vibrational actuator with a structural anisotropy and its control method to diversify the vibrational behavior. We first introduce an analytical model of the proposed actuator. As shown in Fig. 1(c), the actuator comprises a rectangular cross-sectional flexible beam and a rotational-type motor. As the structural anisotropy, the rotational axis of the motor is arranged nonparallel to both principal axes of bending stiffness of the beam. We then theoretically reveal the vibrational phenomenon of the actuator. It is shown that, using the synthetic wave input comprising two sine waves based on the resonance frequencies for the principal axes of the beam, the vibrational orbit of the tip of the beam can be controlled in the same manner as the Lissajous curve. Finally, we show the experimental validation of the proposed

Y. Miyazaki and M. Higashimori are with the Department of Mechanical Engineering, Graduate School of Engineering, Osaka University, Suita 565-0871, Japan. miyazaki@ims.mech.eng.osaka-u.ac.jp, higashi@mech.eng.osaka-u.ac.jp

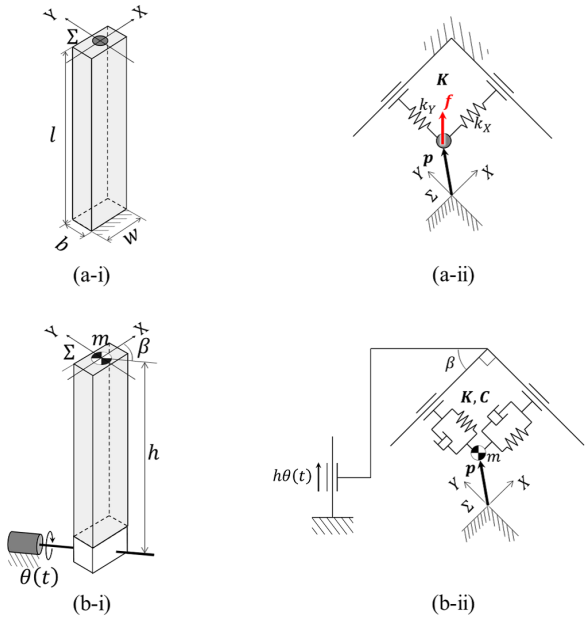

Fig. 2. Analytical model. (a-i) Flexible beam. (a-ii) Linear model for the tip motion of the beam. (b-i) Flexible vibrational actuator. (b-ii) Linear model for the tip motion of the actuator.

method. The Lissajous curve-based vibrational orbit control is performed using a prototype actuator. Furthermore, an application to underactuated-type locomotor is demonstrated.

The rest of this paper is organized as follows. Section II explains the model of the proposed actuator. Section III discusses the control of the vibrational orbit of the actuator. Section IV presents the experimental validation. Finally, Section V describes the conclusions of this work.

II. Vibration Analysis

A. Analytical Model

Fig. 2(b-i) depicts the model of the flexible vibrational actuator. The flexible vibrational actuator constitutes the flexible beam shown in Fig. 2(a-i), a rotational motor connected to the base of the beam, and a mass attached to the tip of the beam. The beam is made of viscoelastic material. The cross-section of the beam is a rectangle. The mass of the beam is assumed to be negligible. The meanings of symbols are as follows.

- Σ_R Base coordinate system. The x_R- and y_R-axes are horizontal.
- Σ Coordinate system moves in conjunction with the root of the rotational motor. The origin is located at the cross-sectional center of the tip of the beam in its natural and vertical state. The X-axis corresponds to the longitudinal direction of the cross-section of the beam and the Y-axis corresponds to the lateral direction of the cross-section of the beam.
- $\boldsymbol{p}$ Position vector expressing the tip of the flexible beam with respect to Σ.
- b Thickness of the flexible beam.
- w Width of the flexible beam.
- l Length of the flexible beam.
- β Twist angle formed by X-axis and the rotational axis of the motor.
- m Mass attached on the tip of the flexible beam.
- h Distance between the rotational axis of the motor and the mass.
- θ Angular displacement of the rotational axis of the motor. When $\theta = 0°$, the beam in natural state is vertical.

B. Statics of Beam

Fig. 2(a-ii) shows the linearized model for the tip part of the flexible beam. According to the theory of mechanics of materials, when a load $\boldsymbol{f} = [F_X, F_Y]^T$ is applied to the tip point of the beam, the displacement of the tip point $\boldsymbol{p} = [p_X, p_Y]^T$ is given by:

$$p_X = \frac{l^3}{3EI_X} F_X,\ p_Y = \frac{l^3}{3EI_Y} F_Y, \tag{1}$$

where E denotes Young's modulus; I_X and I_Y denote moments of inertia to the bending deformation in the X and Y directions, respectively. As the cross section is rectangular, I_X and I_Y are expressed by:

$$I_X = \frac{bw^3}{12},\ I_Y = \frac{b^3 w}{12}. \tag{2}$$

Transforming (1) and substituting (2), we obtain:

$$\boldsymbol{f} = \boldsymbol{K}\boldsymbol{p}, \tag{3}$$

where

$$\boldsymbol{K} = \begin{bmatrix} k_X & 0 \\ 0 & k_Y \end{bmatrix},\ k_X = \frac{Ebw^3}{4l^3},\ k_Y = \frac{Eb^3 w}{4l^3}.$$

$\boldsymbol{K}$ denotes the stiffness matrix for the tip point of the beam due to bending deformation.

C. Dynamics of Actuator

Fig. 2(b-ii) shows the linearized model for the tip part of the bending vibrational actuator. Equations of motion for the tip of flexible beam in the X-Y plane are:

$$m\boldsymbol{I}\ddot{\boldsymbol{p}} + \boldsymbol{C}(\dot{\boldsymbol{p}} - h\boldsymbol{R}^T(\beta)\dot{\boldsymbol{\theta}}) + \boldsymbol{K}(\boldsymbol{p} - h\boldsymbol{R}^T(\beta)\boldsymbol{\theta}) = \boldsymbol{0}, \tag{4}$$

where

$$\boldsymbol{p} = \begin{bmatrix} p_X(t) \\ p_Y(t) \end{bmatrix},\ \boldsymbol{\theta} = \begin{bmatrix} 0 \\ 1 \end{bmatrix} \theta(t),\ \boldsymbol{C} = \alpha\boldsymbol{K},$$
$$\boldsymbol{R}(\beta) = \begin{bmatrix} \cos\beta & -\sin\beta \\ \sin\beta & \cos\beta \end{bmatrix}.$$

$\boldsymbol{C}$ denotes the damping matrix for the tip of the beam due to bending deformation; Viscosity is assumed to be proportional to stiffness and α denotes viscosity proportionality constant [12]; I and $\boldsymbol{R}(\beta)$ denote the unit matrix and rotation matrix. The gravitational torque acting on the beam is assumed to be negligible. Employing the Laplace transform, the frequency transfer functions from the input $\theta(t)$ to the tip position of the beam $\boldsymbol{p}(t)$ are written as:

$$G_X(j\omega) = \frac{P_X(j\omega)}{\Theta(j\omega)} = \frac{h\sin\beta\ (1+\alpha j\omega)\omega_X^2}{(1+\alpha j\omega)\omega_X^2 - \omega^2}, \tag{5}$$
$$G_Y(j\omega) = \frac{P_Y(j\omega)}{\Theta(j\omega)} = \frac{h\cos\beta\ (1+\alpha j\omega)\omega_Y^2}{(1+\alpha j\omega)\omega_Y^2 - \omega^2},$$

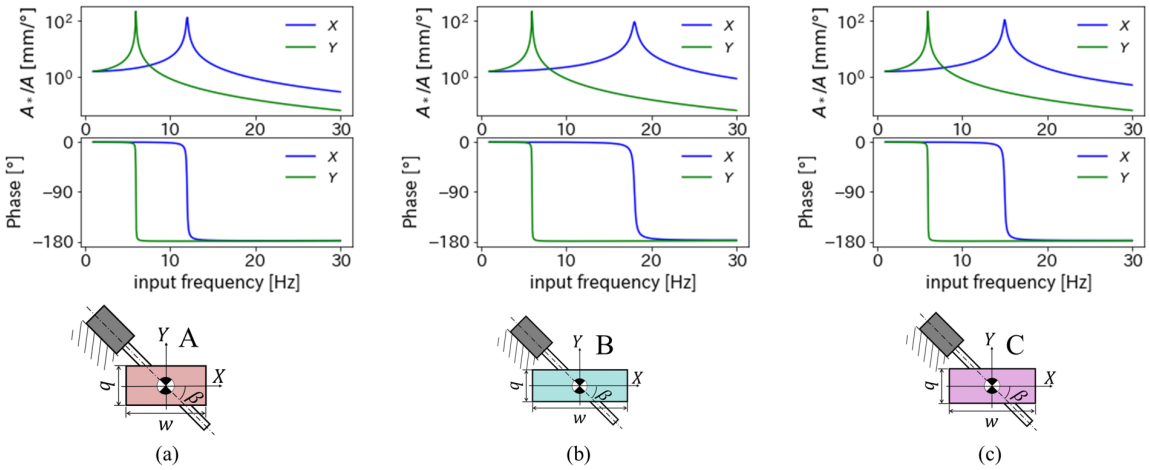

Fig. 3. Frequency response of the flexible vibrational actuator. (a) $f_X : f_Y = 2 : 1$. (b) $f_X : f_Y = 3 : 1$. (c) $f_X : f_Y = 2.5 : 1$.

where

$$\omega_X = \sqrt{\frac{k_X}{m}},\ \omega_Y = \sqrt{\frac{k_Y}{m}}.$$

$P_X(s)$, $P_Y(s)$, and $\Theta(s)$ denote the Laplace transforms of $p_X(t)$, $p_Y(t)$ and $\theta(t)$, respectively; ω_X and ω_Y denote natural frequency; j and ω denote the imaginary unit and input angular frequency, respectively.

When α is sufficiently small, the resonant frequencies f_X and f_Y for vibration in the X and Y directions are:

$$\begin{aligned} f_X &\approx \frac{1}{2\pi}\omega_X = \frac{1}{2\pi}\sqrt{\frac{k_X}{m}} = \frac{w}{4\pi}\sqrt{\frac{ES}{l^3}}, \\ f_Y &\approx \frac{1}{2\pi}\omega_Y = \frac{1}{2\pi}\sqrt{\frac{k_X}{m}} = \frac{b}{4\pi}\sqrt{\frac{ES}{l^3}}, \end{aligned} \tag{6}$$

where $S = bw$ denotes the cross-sectional area of the beam. From (6), we obtain

$$\frac{f_X}{f_Y} \approx \frac{w}{b}, \tag{7}$$

which indicates that the ratio of the resonant frequencies is almost equal to the aspect ratio of the cross-section of the beam.

III. Vibrational Orbit Control

A. Vibrational Orbit of Tip of Flexible Beam

Supposing the following inputs of the rotational motor:

$$\theta_1(t) = A_1 \sin(2\pi f_1 t - \phi_{Y,1}), \tag{8}$$
$$\theta_2(t) = A_2 \sin(2\pi f_2 t - \phi_{X,2} + \phi), \tag{9}$$

the orbits of the tip of the beam for each input are expressed as follows:

$$\boldsymbol{p}_1(t) = \begin{bmatrix} H_{11} \\ H_{21} \end{bmatrix}, \tag{10}$$

$$\boldsymbol{p}_2(t) = \begin{bmatrix} H_{12} \\ H_{22} \end{bmatrix}, \tag{11}$$

$$H_{11} = A_{X,1}\sin(2\pi f_1 t - \phi_{Y,1} + \phi_{X,1}),$$
$$H_{12} = A_{X,2}\sin(2\pi f_2 t + \phi),\ H_{21} = A_{Y,1}\sin(2\pi f_1 t),$$
$$H_{22} = A_{Y,2}\sin(2\pi f_2 t - \phi_{X,2} + \phi_{Y,1} + \phi),$$

where

$$A_{*,i} = A_i|G_*(2\pi j f_i)|,\ \phi_{*,i} = \angle G_*(2\pi j f_i), \tag{12}$$
$$i = \{1, 2\},\ * = \{X, Y\},$$

A_i, f_i, and ϕ denote amplitudes, frequencies, and phase differences of the input, respectively; $\phi_{*,i}$ represents phase differences caused by the flexible structure. By subtracting $\phi_{*,i}$ in advance, these are erased from H_{12} and H_{21}.

According to superposition principle, supposing the following inputs of the rotational motor

$$\theta_{12}(t) = \theta_1(t) + \theta_2(t), \tag{13}$$

the orbits of the tip of the beam for each input are expressed as follows:

$$\boldsymbol{p}_{12}(t) = \boldsymbol{p}_1(t) + \boldsymbol{p}_2(t) = \begin{bmatrix} H_{11} + H_{12} \\ H_{21} + H_{22} \end{bmatrix}. \tag{14}$$

B. Lissajous Curve-based Orbit Control

Actuators A, B, and C with ratios of resonant frequencies of $f_X : f_Y = 2 : 1$, $f_X : f_Y = 3 : 1$, and $f_X : f_Y = 2.5 : 1$ are displayed in Figs. 3(a), (b), and (c), respectively. Resonant frequencies in the Y direction, twist angle, distances between the rotational axis of the motor and the mass, and the viscosity proportionality constant are $f_Y = 6$ Hz, $\beta = 45°$, $h = 125$ mm, and $\alpha = 1.5 \times 10^{-4}$ s. Providing the motor of actuator A with a sine wave input $\theta(t) = \theta_1(t)$ of $f_1 = f_Y$, $A_1 = 0.1°$, the orbit $\boldsymbol{p}_1(t)$ shown

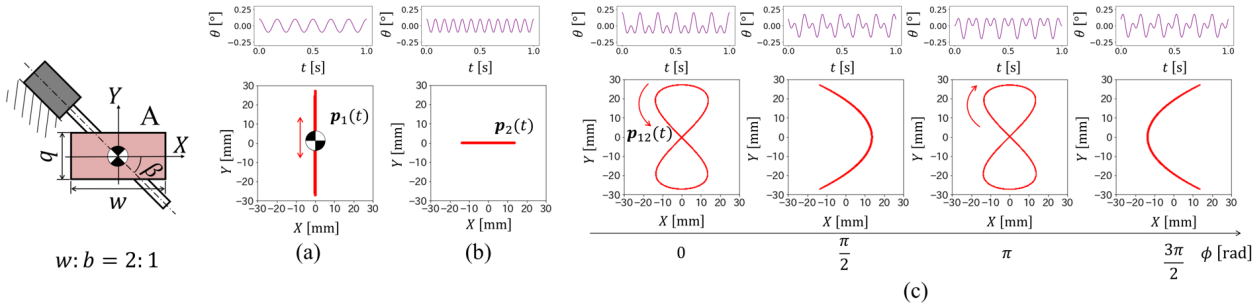

Fig. 4. Lissajous curve-based orbit control in the actuator A ($f_X : f_Y = 2 : 1$). (a) Sine wave with f_Y. (b) Sine wave with f_X. (c) Synthetic waves with f_Y and f_X.

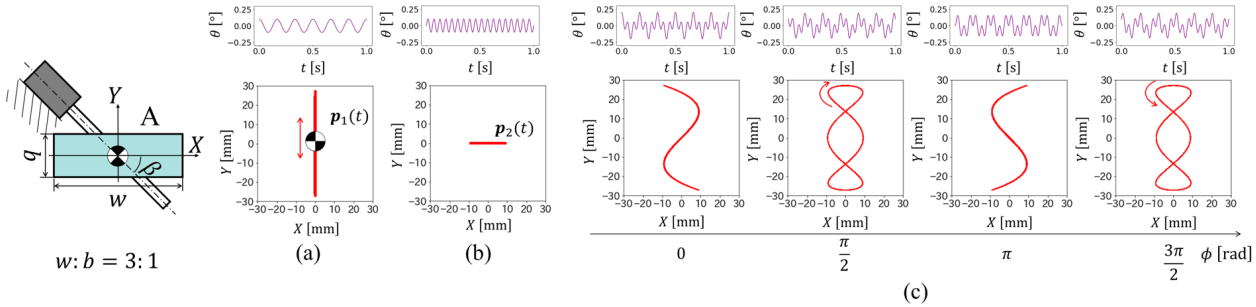

Fig. 5. Lissajous curve-based orbit control in the actuator B ($f_X : f_Y = 3 : 1$). (a) Sine wave with f_Y. (b) Sine wave with f_X. (c) Synthetic waves with f_Y and f_X.

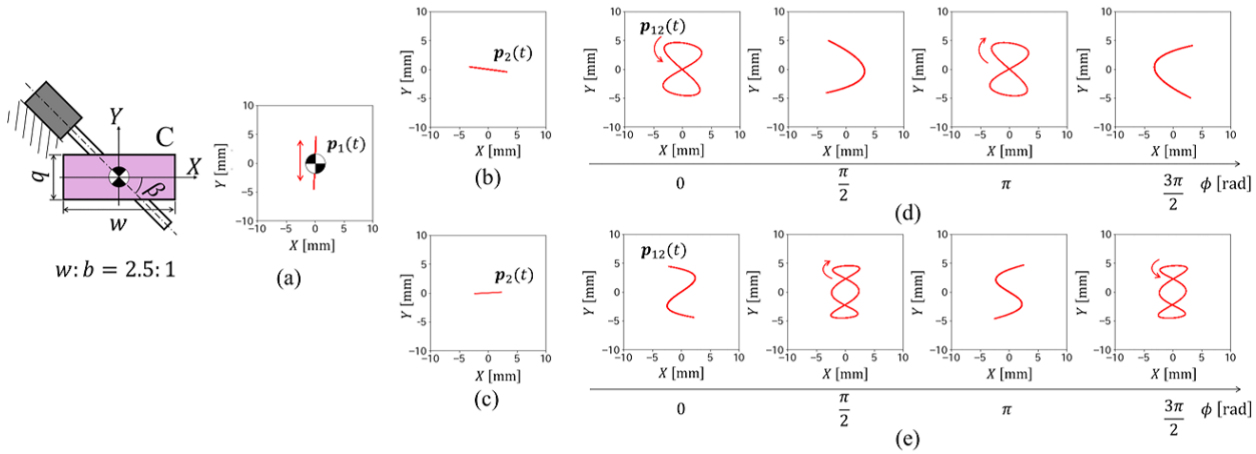

Fig. 6. Lissajous curve-based orbit control in the actuator C ($f_X : f_Y = 2.5 : 1$). (a) Sine wave with f'_Y. (b) Sine wave with $f'_{X,1}$. (c) Sine wave with $f'_{X,2}$. (d) Synthetic wave with f'_Y and $f'_{X,1}$. (e) Synthetic wave with f'_Y and $f'_{X,2}$.

in Fig. 4(a) is obtained. As $|G_Y(2\pi j f_1)| \gg |G_X(2\pi j f_1)|$, $\boldsymbol{p}_1(t)$ is almost parallel to the Y-axis. Providing the motor of actuator A with a sine wave input $\theta(t) = \theta_2(t)$ of $f_2 = 2f_1 (= f_X)$, $A_2 = 0.1°$, the orbit $\boldsymbol{p}_2(t)$ shown in Fig. 4(b) is obtained. As $|G_X(2\pi j f_2)| \gg |G_Y(2\pi j f_2)|$, $\boldsymbol{p}_2(t)$ is almost parallel to the X-axis. Providing the motor of the actuator A with a synthetic wave input $\theta(t) = \theta_{12}(t)$ of $f_1 = f_Y$, $A_1 = 0.1°$, $f_2 = 2f_1 (= f_X)$ $A_2 = 0.1°$, the orbits $\boldsymbol{p}_{12}(t)$ shown in Fig. 4(c) is obtained. As $\boldsymbol{p}_{12}(t)$ is coupled vibation in two orthogonal directions $\boldsymbol{p}_1(t)$ and $\boldsymbol{p}_2(t)$, the shape of $\boldsymbol{p}_{12}(t)$ is a Lissajous curve for frequency ratio $2 : 1$ and phase difference ϕ. Similarly, providing the motor of the actuator B with a sine wave input $\theta(t) = \theta_1(t)$ of $f_1 = f_Y$, $A_1 = 0.1°$, the orbit $\boldsymbol{p}_1(t)$ shown in Fig. 5(a) is obtained, and providing the motor of the actuator B with a sine wave input $\theta_2(t)$ of $f_2 = 3f_1 (= f_X)$, $A_2 = 0.1°$, the orbit $\boldsymbol{p}_2(t)$ shown in Fig. 5(b) is obtained. Providing the motor of actuator B with a synthetic wave input $\theta(t) = \theta_{12}(t)$ of $f_1 = f_Y$, $A_1 = 0.1°$, $f_2 = 3f_1 (= f_X)$, $A_2 = 0.1°$, the orbit $\boldsymbol{p}_{12}(t)$ shown in Fig. 5(c) is obtained, which is the shape of a Lissajous curve for the frequency ratio $3 : 1$ and phase difference ϕ.

Next, we considered formation of both types of Lissajous curve-based orbits with the same actuator. Providing the motor of the actuator C with a sine wave input $\theta(t) = \theta_1(t)$ of $f_1 = f'_Y = 5.9$ Hz $\approx f_Y$, $A_1 = 0.1°$, the orbit $\boldsymbol{p}_1(t)$ shown in Fig. 6(a) is obtained. Providing the motor of the actuator C with sine wave input $\theta(t) = \theta_2(t)$ of $f'_{X,1} = 2f'_Y$, $A_2 = 0.8°$

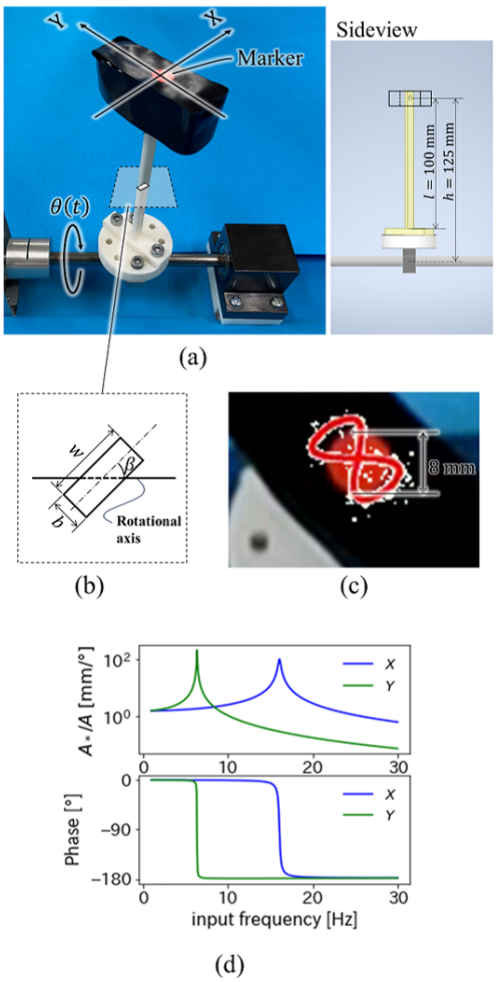

Fig. 7. Experimental setup. (a) Overview. (b) Cross-section of the beam. (c) Trajectory of the marker on the tip. (d) Frequency response.

and of $f'_{X,2} = 3f'_Y$, $A_2 = 0.6°$, the orbits $\boldsymbol{p}_2(t)$ shown in Fig. 6(b) and Fig. 6(c) are obtained, respectively. Providing the motor of actuator C with a synthetic wave input $\theta(t) = \theta_{12}(t)$ of $f_1 = f'_Y$, $A_1 = 0.1°$, $f_2 = f'_{X,1}$, $A_2 = 0.8°$ and $f_1 = f'_Y$, $A_1 = 0.1°$, $f_2 = f'_{X,2}$, $A_2 = 0.6°$, the orbits $\boldsymbol{p}_{12}(t)$ shown in Fig. 6(d) and Fig. 6(e) are obtained. As orbits $\boldsymbol{p}_1(t)$ shown in Fig. 6(a) and $\boldsymbol{p}_2(t)$ shown in Fig. 6(b) and orbit $\boldsymbol{p}_1(t)$ shown in Fig. 6(a) and $\boldsymbol{p}_2(t)$ shown in Fig. 6(c) are nearly orthogonal to each other, respectively, the vibrational orbit shapes of $\boldsymbol{p}_{12}(t)$ shown in Fig. 6(d) and (e) are Lissajous curves for frequency ratio $2:1$ and $3:1$.

As described above, through designing the resonant frequencies of the beam and applying appropriate synthetic wave inputs, Lissajous curve-based vibrational orbits at the tip of the beam of the flexible vibrational actuator can be controlled.

IV. Experiments

The orbit control and its application to locomotion were experimentally demonstrated. The supplementary video file shows experiments.

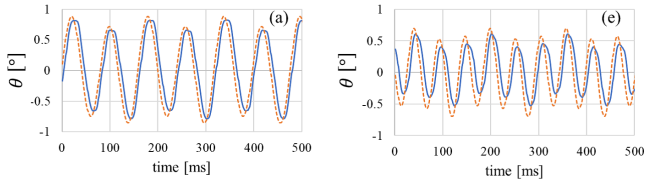

Fig. 8. Examples of the input angle $\theta(t)$ in the steady state. Orange and blue lines show the target and actual angles, respectively. (a) Parameters$\gamma = 2, \varepsilon = 8, \phi = 0$ are same as ones in Fig. 9(a). (b) Parameters of $\gamma = 3, \varepsilon = 6, \phi = 0$ are same as ones in Fig. 9(e).

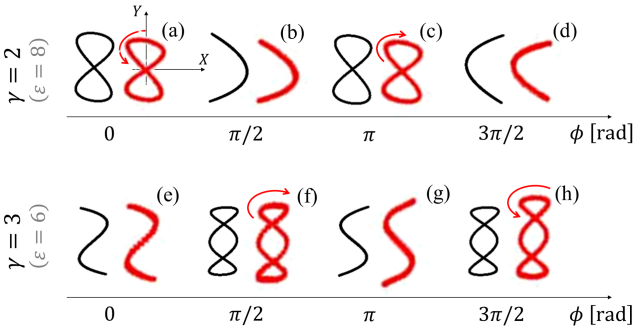

Fig. 9. Experimental results. Black line: Lissajous curve drawn by analytical model. Red line: Lissajous curve drawn in experiment.

A. Flexible Vibrational Actuator

Fig. 7(a) presents an overview of the experimental setup. The flexible beam is made of polylactic acid (PLA) by 3D printing. The Young's modulus and the viscosity proportionality constant were empirically estimated to be $E = 2.5$ GPa and $\alpha = 1.5 \times 10^{-4}$ s through experiments. The parameters of the actuator are: $b = 2.6$ mm, $w = 6.5$ mm, $l = 100$ mm, $h = 125$ mm, $\beta = 45°$, $m = 50$ g. Fig. 7(b) shows the cross-sectional view. As shown in Fig. 7(c), the orbit of the tip of the beam was recorded using a camera with 400 fps. The two resonant frequencies were measured as $f_X = 16.06$ Hz, $f_Y = 6.38$ Hz ($f_X/f_Y \approx 2.5$). Accordingly, the frequency transfer functions $G_X(j\omega)$ and $G_Y(j\omega)$ were calculated. Fig. 7(d) presents the frequency response of the actuator. The angular displacement input of rotational motor is given by:

$$\begin{aligned}\theta(t) = & \quad A_1 \sin(2\pi f_1 t - \phi_{Y,1}) \\ & + \quad A_2 \sin(2\pi f_2 t - \phi_{X,2} + \phi).\end{aligned} \tag{15}$$

Fig. 8 shows examples of the input angle of the rotational motor in the steady state. The input frequency and amplitude of the first sine wave are $f_1 = 6.3$ Hz and $A_1 = 0.1°$. The frequency ratio $\gamma = f_2/f_1$ and the amplitude ratio $\varepsilon = A_2/A_1$ of the input are defined. The phase differences caused by the flexible structure were estimated to be $\phi_{Y,1} = -0.23$ rad, $\phi_{X,2} = -0.02$ rad for $\gamma = 2$, and $\phi_{Y,1} = -0.23$ rad, $\phi_{X,2} = -3.08$ rad for $\gamma = 3$. Fig. 9 displays representative orbits for the γ, ε, and ϕ. The red lines show the experimental orbits and the black lines show the theoretical orbits. By changing γ, two types of Lissajous curve, $2:1$ and $3:1$, can be realized, and the change in form by ϕ can also be observed. The theoretical and experimental results are in qualitative agreement.

B. Application to Underactuated Locomotor

The flexible vibrational actuator was further applied to locomotion. Fig. 10 shows the locomotor equipped with the actuator. The robot has four feet and weighs 388.0 g. The parameters of the actuator are: $b = 2.0$ mm, $w = 8.0$ mm, $l = 100$ mm, $h = 130$ mm, $m = 64$ g, $\beta = 30°$. The beam is made of polylactic acid (PLA) by 3D printing. Mass m is suspended at a height of approximately 40 mm. The angular displacement input is as follows:

$$\theta(t) = A\sin(2\pi ft) + \varepsilon A\sin(2\pi\gamma ft + \psi), \tag{16}$$

where ψ is the phase difference of input. When the parameters were tuned, several characteristic behaviors of the robot were found. Fig. 11 shows the behaviors of the robot with respect to the input parameters γ, f, A, ε, ψ. Each position of the robot was captured every 10 s. The vibration reaction transmitted to the rotational motor causes slip between the feet and the ground. Controlling timing and direction of the slip, the actuation curves lead to the particular locomotions.

The experimental results are discussed with a focus on symmetry. Lissajous curve with frequency ratio $2:1$ has X-axis symmetry. Therefore, assuming isotropic structure of the main body of the robot, it is expected that the Lissajous curve-based orbit with frequency ratio $2:1$ only moves the robot in the X direction as this is the only motion that does not break the X-axis symmetry. In addition, the Lissajous curve with frequency ratio $3:1$ has twice rotation symmetry. Therefore, assuming isotropic structure of the main body of the robot, it is expected that the Lissajous curve-based orbit with frequency ratio $3:1$ only rotates the robot around its center because only this motion does not break the twice rotation symmetry. Furthermore, changing the phase difference by π rad, the Lissajous curves with frequency ratios $2:1$ and $3:1$ become Y-axis inversed and mirror image reversal. Thus, changing ψ by π rad is expected to reverses the motion of the robot. The experimental results are not perfectly symmetrical due to the incompleteness of the Lissajous curve-based orbit and the anisotropy of friction between the four feet and the ground. However, the motion changed with respect to the vibrational orbit was experimentally confirmed. As detailed above, utilizing the vibrational orbit control method, three-DOF motion of the robot can be generated using only one motor.

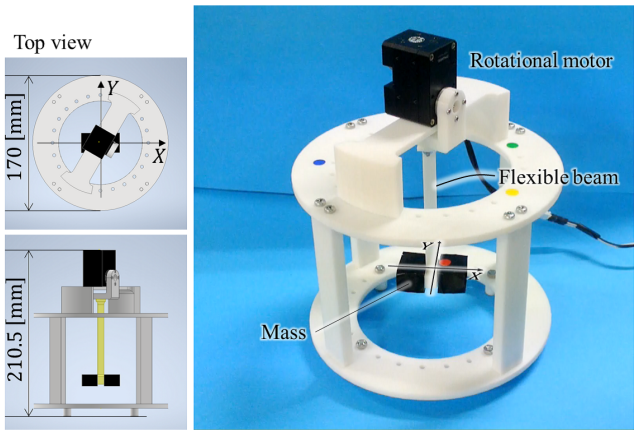

Fig. 10. A prototype of underactuated locomotor. The proposed flexible vibrational actuator is installed at roof of the robot.

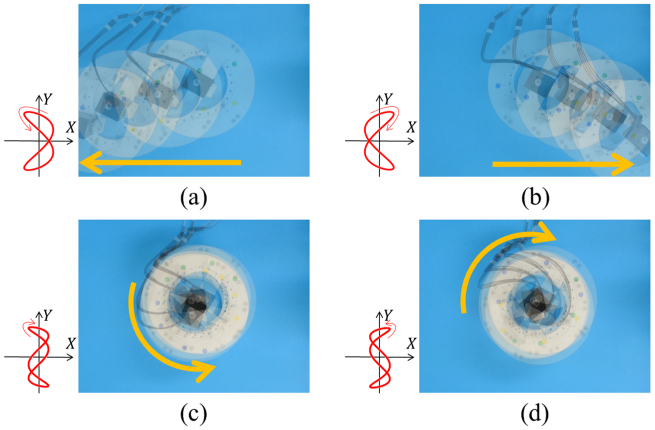

Fig. 11. Locomotion of the developed robot and outlines of actuation curves. According to the Lissajous curve-based orbit control, the robot motion changes. Three-DOF motion of the robot can be generated using only one motor. (a) Translational motion to the left by $\gamma = 2$, $f = 4.6$ Hz, $A = 1.1°$, $\varepsilon = 2.3$, $\psi = -0.2$ rad. (b) Translational motion to the right by $\gamma = 2$, $f = 4.6$ Hz, $A = 1.1°$, $\varepsilon = 2.3$, $\psi = -0.2 + \pi$ rad. (c) Rotational motion to the counterclockwise direction by $\gamma = 3$, $f = 4.6$ Hz, $A = 1.0°$, $\varepsilon = 3.0$, $\psi = 1.0$ rad. (d) Rotational motion in the clockwise direction by $\gamma = 3$, $f = 4.6$ Hz, $A = 1.0°$, $\varepsilon = 3.0$, $\psi = 1.0 + \pi$ rad.

V. Conclusion

This paper proposed a novel flexible vibrational actuator with a structural anisotropy and its control method to diversify the vibrational behavior. The main results are summarized as follows:

- The analytical model of the proposed actuator, which comprises a rectangular cross-sectional flexible beam and a rotational motor, was introduced. As the structural anisotropy, the rotational axis of the motor is nonparallel to both principal axes of bending stiffness of the beam.
- The vibrational phenomenon of the actuator was theoretically revealed: using the synthetic wave input comprising two sine waves based on the resonance frequencies for the principal axes of the beam, the vibrational orbit of the tip of the beam can be controlled in the same manner as the Lissajous curve.
- The proposed method was experimentally validated. The Lissajous curve-based vibrational orbit control was performed using a prototype actuator. Furthermore, an application to underactuated-type locomotor was demonstrated.

Future works include consideration of external interactions such as vibration of the base of the actuator, contact force between the beam, environment, and aerodynamic drag. In addition, an extension to the three-dimensional vibration problem will be discussed. Furthermore, several insects, such as bees, flies, and *Paratuposa placentis* are known to have a figure-eight wing trajectory [13]. We would like to extend the theory to diverse types of robots in the context of biomimetics.

REFERENCES

[1] S. Kim, C. Laschi and B. Trimmer: "Soft Robotics: A Bioinspired Evolution in Robotics," Trends in Biotechnology, vol. 31, no. 5, pp. 287–294, 2013.

[2] M. Manti, V. Cacucciolo, and M. Cianchetti: "Stiffening in Soft Robotics: A Review of the State of the Art," IEEE Robotics and Automation Magazine, vol. 23, iss. 3, pp. 93–106, 2016.

[3] D. Rus and M.T. Tolley: "Design, Fabrication and Control of Soft Robots," Nature, vol. 521, no. 7553, pp. 467–475, 2015.

[4] J.Z. Gul, M. Sajid, M.M. Rehamn, G.U. Siddiqui, I. Shah, K.-H. Kim, J.-W. Lee, and K.H. Choi: "3D Printing for Soft Robotics. A Review," Science and Technology of Advanced Materials, vol. 19, no. 1, pp. 243–262, 2018.

[5] F.L. Moro, N.G. Tsagarakis, and D.G. Caldwell: "Walking in the resonance with the COMAN robot with trajectories based on human kinematic motion primitives (kMPs)," Autonomous Robots, vol. 36 pp. 331–347, 2014.

[6] K. Arakawa, F. Giorgio-Serchi and H. Mochiyama: "Snap Pump: A Snap-Through Mechanism for a Pulsatile Pump," in IEEE Robotics and Automation Letters, vol. 6, no. 2, pp. 803–810, 2021.

[7] S. Iyobe, M. Shimizu and T. Umedachi: "Diverse Behaviors of a Single-Motor-Driven Soft-Bodied Robot Utilizing the Resonant Vibration of 2D Repetitive Slit Patterns," in IEEE Robotics and Automation Letters, vol. 7, no. 2, pp. 992–999, 2022.

[8] Y. Jiang, F. Chen, and D.M. Aukes: "Tunable Dynamic Walking via Soft Twisted Beam Vibration," IEEE Robotics and Automation Letters, vol. 8, no. 4, pp. 1967–1974, 2023.

[9] M. Sharifzadeh and D.M. Aukes: "Curvature-Induced Buckling for Flapping-Wing Vehicles," in IEEE/ASME Transactions on Mechatronics, vol. 26, no. 1, pp. 503–514, 2021.

[10] D. Kim, Z. Hao, J. Ueda, and A. Ansari: "A 5mg micro-bristle-bot fabricated by two-photon lithography," Journal of Micromechanics and Microengineering, vol. 29, no. 10, pp. 105006, 2019.

[11] A. Maruo, A. Shibata, and M. Higashimori: "Dynamic Underactuated Manipulator Using a Flexible Body with a Structural Anisotropy," Proc. IEEE Int. Conf. on Robotics and Automation, pp. 7117–7123, 2022.

[12] T.K. Caughey, and M.E.J. O'Kelly: "Classical Normal Modes in Damped Linear Dynamic Systems,"ASME Journal of Applied Mechanics, vol. 32, no.3, pp. 583–588, 1965.

[13] S.E. Farisenkov, D. Kolomenskiy, and P.N. Petrov *et al.*: "Novel flight style and light wings boost flight performance of tiny beetles," Nature, vol. 602, pp. 96–100, 2022.